Atomistic modelling of iodine-oxygen interactions in strained sub-oxides of zirconium

V. Podgurschi[a,1], D. J. M. King[a,2], J. Smutna[a,3], J. R. Kermode[b,4], M. R. Wenman[a,*]

[a]*Department of Materials and Centre for Nuclear Engineering, Imperial College London, Exhibition Road, London, SW7 2AZ, United Kingdom of Great Britain and Northern Ireland*
[b]*Warwick Centre for Predictive Modelling, School of Engineering, University of Warwick, Coventry CV4 7AL, United Kingdom of Great Britain and Northern Ireland*

Abstract

In water reactors, iodine stress corrosion cracking is considered the cause of pellet-cladding interaction failures, but the mechanism and chemistry are debated and the protective effect of oxygen is not understood. Density functional theory calculations were used to investigate the interaction of iodine and oxygen with bulk and surface Zr under applied hydrostatic strain (-2 % to +3 %) to simulate crack tip conditions in Zr to ZrO_2, using a variety of intermediate suboxides (Zr_6O, Zr_3O, Zr_2O and ZrO). The formation energy of an iodine octahedral interstitial in Zr was found to decrease with increasing hydrostatic strain, whilst the energy of an iodine substitutional defect was found to be relatively insensitive to strain. As the oxygen content increased, the formation energy of an iodine interstitial increased from 1.03 eV to 8.61 eV supporting the idea that oxygen has a protective effect. At the same time, a +3 % tensile hydrostatic strain caused the iodine interstitial formation energy to decrease more in structures with higher oxygen content: 4.56 eV decrease in ZrO compared to 1.47 eV decrease for pure Zr. Comparison of the substitutional and interstitial energies of iodine, to the adsorption energy of iodine, in the presence of oxygen, shows the substitutional energy of iodine onto a Zr site is more favourable for all strains and even interstitial iodine is favourable between strains of +1-5%. Although substitutional defects are preferred to octahedral interstitial defects, in the ordered suboxides, a 3 % tensile strain significantly narrows the energy gap and higher strains could cause interstitial defects to form.

---

[*]Corresponding author
    Email address: m.wenman@imperial.ac.uk (M. R. Wenman)
[1]vlad.podgurschi12@imperial.ac.uk
[2]daniel.king@imperial.ac.uk
[3]jana.smutna12@imperial.ac.uk
[4]j.r.kermode@warwick.ac.uk

1. Introduction

Zirconium (Zr) alloys are often used for nuclear fuel cladding due to their good resistance to corrosion and excellent neutron transparency. Pellet cladding interaction (PCI) is a phenomenon that occurs between the inner surface of the nuclear fuel cladding and the outer surface of the fuel when they come into contact. This occurs during power transients, in incidental transients as well as during steady state operation. PCI is developed by fuel-pellet relative motion, and can also manifest itself through stress corrosion cracking (SCC) of the cladding in the presence of volatile fission products such as iodine (I-SCC) [1, 2, 3]. In pressurised water reactors (PWR) using unlined Zr alloy cladding and UO_2 fuel, I-SCC has been suggested to be the main cause of PCI failures [4, 5]. The complete I-SCC mechanism, however, is not yet fully understood; the chemistry of the attacking species and the oxygen's chemistry are still subject to debate [6]. Iodine has been suggested to create intermediate Zr-I-Zr bonds that break easier than the Zr-Zr bonds or to pin dislocations thus limiting plastic deformation ahead of the crack tip [7].

Extensive experimental work has been performed but due to the timescale involved with an SCC process, direct observations can be difficult, especially given the added effect of irradiation of the material. Consequently, computational simulations have been used to study the role of iodine and other chemical species in zirconium or zirconium alloy cladding. In previous work by Legris and Domain [8], density functional theory (DFT) calculations were performed to investigate iodine-zirconium interactions. Tu et al. [9] used DFT calculations and nudged elastic band (NEB) methods to study the formation energy and migration energy barriers of a number of iodine defects in bulk zirconium and found that the main diffusion mechanisms occurred via the iodine interstitial sites as well as substitution on zirconium sites and zirconium vacancies. The effect of strain was not investigated. Strain effects on oxygen migration in zirconium were modelled by Liu et al. [10] who showed that compressive strains slowed down diffusion. Thus far, work on iodine defect formation energies and diffusion has only been conducted on bulk strain free systems. While previous work yielded important results regarding the interactions between iodine and zirconium, it did so by only considering unstrained bulk zirconium crystals. During the I-SCC process the crack tip atomic environment is under triaxial tension. It has been suggested that due to the relatively high iodine

2

incorporation energies, I-SCC is more likely to be caused by iodine adsorption and diffusion along the surfaces of the open crack [6, 11]. At the same time, iodine has recently been experimentally observed both at the crack tip and ahead of it [12, 13]. In the current study, we assume the latter to be true and examine the behaviour of iodine in bulk structures in equilibrium and in strained environments and to some degree compare to surface environments.

Oxygen has been shown experimentally to increase the resistance to I-SCC due to the protective ZrO_2 layer formed [14]. Furthermore, it has been shown that even if the cladding is in tension, as long as the ZrO_2 layer is intact, I-SCC does not occur [15, 16, 17, 18, 19, 20, 21]. Nonetheless, it has also been suggested that ZrO forms when oxygen is less readily available [22, 23]. Due to the oxygen gradient into the metal below the oxide layer, even if the oxide does fracture, it is unlikely that iodine will come into contact with pure Zr. Instead, it will most likely interact with some metallic structures containing oxygen. Once the oxide film on the zirconium metal or alloy surface forms, oxygen atoms from the film can diffuse into the bulk metal. The process has been studied through both experimental and computational studies [24, 25, 26, 27, 28, 10]. At the oxide-metal interface of Zr alloys several structures have been identified. Hu et al. [22] used transmission electron microscopy, scanning transmission electron microscopy, transmission-electron back scatter diffraction and electron energy loss spectroscopy to analyse the interface and identified local regions of hexagonal ZrO, tetragonal and monoclinic ZrO_2 confirming earlier modelling work by Nicholls et al. [29]. Ordered suboxides such as ZrO, Zr_2O, Zr_3O and Zr_6O [30, 31] have also been identified at the metal-oxide interface [32, 33, 23]. Kenich et al. [34] used DFT calculations to produce Brouwer diagrams of tetragonal ZrO_2 containing iodine and showed that there is a competition between iodine and oxygen for anion sites in zirconia. The competition is both phase and oxygen pressure dependent. For high oxygen partial pressure in the tetragonal phase of ZrO_2, the oxygen was found to compete with iodine for anion sites. It is not currently known how the various suboxide structures affect iodine behaviour in Zr metal and yet understanding how iodine interacts with Zr when oxygen is less available must be important to understanding PCI. Therefore, it is the purpose of this study to examine the effect of strain on the behaviour of iodine in Zr with varying levels of oxygen found at the metal free surfaces.

2. Method

2.1. Bulk Systems DFT Calculations

To show that large (order of 1-10%) crack tip elastic strains are theoretically possible in zirconium, edge cracks were investigated in pure single crystal zirconium slabs using a hybrid (quantum mechanics/molecular mechanics) QM/MM method introduced by [35, 36]. The crack plane was on the basal plane and the crack front was parallel to the $[\bar{1}010]$ direction. The crack growth direction was chosen to be $[1\bar{2}10]$. Periodic boundary conditions were applied in the z direction. The dimensions along the x, y and z axis corresponded to approximately 1200 Å, 600 Å and 6 Å respectively. Given the small thickness (z direction) of the model, the slab was under plane-strain conditions (ϵ_{zz}) = 0. When under tensile stress, a typical strain map for an atomically sharp crack in the y (mode I opening) direction is shown in Figure 1. At the tip, elastic strains (ϵ_{yy}) of up to 17% are possible without any slip or twinning emission (i.e. no form of permanent deformation).

Calculations were first performed on typical crack tip configurations (Figure 2) extracted from the system shown in Figure 1. The crack tip configurations were taken from QM/MM simulations [35, 36]. The two positions chosen were both octahedral interstitial positions having different ϵ_{yy} values (0.16 for Position 1 and 0.05 for Position 2). In both cases the crack was subject to the same energy release rate, G, of 3.0 J m^{-2}. Calculations were then extended to bulk zirconium and ordered zirconium oxygen suboxides supercells in order to do a more thorough parametric study on the effects of strain on defect formation energies. Hydrostatic strain was used for ease of comparisons made between the various sub-oxide structures encountered at the crack tip. For bulk zirconium, QM calculations were performed on the supercells under an applied hydrostatic strain (-2% to 3%) where positive values are tensile. The suboxide structures were first volume optimised. The 3 % hydrostatic strain was then applied and an iodine atom added to the system. Geometry relaxation was then performed while keeping the volume fixed. Effectively, the volume and cell dimensions were fixed for both the zirconium bulk cells and the ordered suboxides and the atoms were allowed to relax.

A DFT method implemented in the CASTEP package [37] was used for all calculations. The generalised gradient approximation (GGA) exchange-correlation functional as formulated by Perdew, Burke and Ernzerhof (PBE) was used. A conjugate gradient method was used to minimize the Hellmann-Feynman forces during relaxations. The convergence criteria used were 10^{-6} eV, 10^{-5}

4

eV/atom, 0.0005 Å and 0.01 eV/Å for the total energy, free energy per atom, ionic displacement and ionic force respectively. A cut-off energy of 400 eV was used. Spin polarisation was used in all calculations. For bulk zirconium, a 5×5×3 supercell with 150 Zr atoms was used in order to minimise the self-interaction energy of the defect across periodic cells and to keep the dimensions as cubic as possible. For the Zr_6O, Zr_3O, Zr_2O and ZrO suboxides, 3×3×3, 3×3×3, 3×3×3 and 3×3×5 supercells with 189, 216, 243 and 270 atoms were used respectively. For all the systems considered, larger supercells were used in order to prevent significant self-interaction of the iodine defect. A 3×3×3 Monkhorst Pack mesh (corresponding to a K-point spacing of 0.03 Å^{-1}) was used for all geometric relaxations. A cold smearing scheme with a width of 0.1 eV was used for the Fermi-surface smearing. Dispersion forces corrections have not been taken into account in the current work and would be of interest for future study.

Given the prevailing theory that iodine will remain on the surface of Zr through an adsorption and diffusion mechanism, adsorption calculations were performed. Here, complete monolayer ($\Theta = 1$) adsorption of O, iodine and a mixture of the two, on the surface face centred cubic (SFCC) sites of the [0001] 2×2 Zr surface was investigated as a function of strain, similar to past work [38]. A 7-layer slab was used with the position of the atoms in the bottom 4 layers being fixed. A vacuum region of 20 Å was used to minimise the interaction of periodic slabs. Formation energies using an isolated iodine and diatomic I_2 molecule, as reference, were calculated to quantify the effect of reference state. Bond population analysis was also performed on the bulk systems and the method is explained in more detail in Section 2.4.

2.2. Defect Formation Energies

The formation energies of interstitial and substitutional defects were calculated. Structures with an octahedral interstitial iodine defect and a substitutional iodine atom on a Zr site were made. Only single octahedral interstitials were considered due to the large atomic size of iodine and the octahedral defect having a lower formation energy (values are presented in the Results section).

The formation energy for an iodine interstitial defect was defined as:

$$E_{(int\ defect)} = E_{(Structure+I)} - E_{Structure} - E_I$$

(1)

where $E_{(Structure+I)}$ is the total energy of a structure supercell with an iodine interstitial atom, $E_{structure}$ is the total energy of the structure supercell without any iodine atoms and E_I is the

ground state energy of an iodine atom in a box of the same dimensions as the one used for the supercell.

Similarly, the iodine substitutional defect energy is defined in Equation 2 as

$$E_{sub} = E_{(Zr-1),I} - \frac{n-1}{n}E_{Zr} - E_I$$

(2)

where $E_{(Zr-1),I}$ is the total energy of a Zr supercell with an iodine atom substituting for a Zr atom, E_{Zr} is the total energy of a Zr supercell without any iodine atoms, E_I is the ground state energy of a single isolated iodine atom and n is the number of Zr atoms.

For the suboxides considered in this work, the substitutional defect formation energy is defined by Equation 3. For example, for an iodine substitutional defect on a Zr site in the Zr_3O 3×3×3 supercell containing 216 atoms, the doped cell refers to the cell having an iodine atom on a Zr site (161 Zr atoms, 54 O and 1 I), the neighbouring phase refers to the pure Zr atoms in that phase (162 Zr), the neighbouring phase with dopant refers to only the Zr atoms with one iodine substituting for a Zr atom (161 Zr atoms, 1 I) and the pristine cell refers to the pure Zr_3O structure (162 Zr atoms, 54 O)

$$E_{sub\ defect} = (E_{doped\ cell} + E_{neighbouring\ phase}) - (E_{neighbouring\ phase\ with\ dopant} + E_{pristine\ cell})$$

(3)

For the surface adsorption calculations, Equation 4 was used for oxygen and iodine onto the SFCC sites of the 0001 (2x2) Zr surface. Similar to past calculations [39]

$$E_{I\ ads} = E_{Zr\ surf\ +\ I} - (E_I + E_{Zr\ surf})$$

(4)

Furthermore, in order to compare the energy of a single iodine interstitial or substitutional defect in bulk Zr versus a Zr surface, Equations 5 and 6 were used where a negative energy change would indicate a lower energy of formation on the surface.

$$\Delta E = (E_{Zr\ bulk} + E_{Zr\ surf,\ I}) - (E_{Zr\ bulk,\ I\ int} + E_{Zr\ surf})$$

(5)

6

$$\Delta E = (E_{\text{Zr bulk}} + E_{\text{Zr surf, I}}) - (E_{\text{Zr bulk, I sub}} + E_{\text{Zr surf}} + \frac{1}{N}E_{\text{Zr bulk}}) \qquad (6)$$

2.3. Ordered Suboxide Structures Considered

In order to analyse the effect of oxygen on the energy of iodine as an octahedral interstitial defect or substitutional defect on a zirconium site, ordered suboxide structures were considered. The ordered suboxides Zr_6O (R$\bar{3}$), Zr_3O (R$\bar{3}$c), Zr_2O (P$\bar{3}$1m) and ZrO (P$\bar{6}$2m) were considered [30, 40] as they have stable phases [41] and are predicted to exist. The defect formation energies were calculated for both unstrained and 3 % tensile hydrostatically strained structures.

Zr_6O has three different octahedral interstitial positions where an iodine atom can be placed. The three positions will be referred to as Zr_6O-1, Zr_6O-2 and Zr_6O-3 respectively in the order that they appear in Figure 3. For the Zr_6O ordered suboxide a 3×3×3 supercell with 241 atoms was used.

The Zr_3O structure has only a single octahedral interstitial position where an iodine atom can be placed (Figure 4) that will be referred to as Zr_3O-1. For the Zr_3O ordered suboxide a 3×3×3 supercell with 216 atoms was used.

The Zr_2O structure has two different octahedral interstitial positions where an iodine can be placed. The two positions will be referred to as Zr_2O-1 and Zr_2O-2 respectively in the order that they appear in Figure 5. For the Zr_2O ordered suboxide a 3×3×3 supercell with 189 atoms was used.

The hexagonal ZrO structure with P$\bar{6}$2m symmetry [29] has four different interstitial (not octahedral) positions where the iodine atom can be placed. The four positions are shown in Figure 6 and are referred to as ZrO-1, ZrO-2, ZrO-3 and ZrO-4 respectively. The ZrO-4 was chosen for further study as it had a significantly lower interstitial defect formation energy compared to the other positions.

2.4. Bond Population Analysis

Mulliken charge and population analysis was performed in order to analyse the bonding properties of the structures. The plane-wave states are projected onto a localised basis set [42] and the population analysis is done using the Mulliken formalism as described by Segall et al. [43, 44]. The bonds analysed were classified based on their proximity and bonding with the iodine interstitial

7

defect. Figure 7 illustrates the concept using the Zr_2O structure but the method is applicable to all structures (except for the pure Zr structure which did not contain any O atoms). The bonds that contain an atom that is close to the defect (i.e. the iodine atom has a bonding contribution with either or both) are termed *I-bonded*. The bonds that do not contain an atom that is close to the defect (i.e. the iodine atom does not have a bonding contribution with either) are termed *non I-bonded*.

3. Results and Discussion

3.1. Benchmarking against existing literature

The interstitial formation energy of iodine in bulk zirconium was previously calculated by Legris and Domain [8], Tu et al. [9] and Han et al. [45] whilst the substitutional energy of iodine in bulk zirconium was previously calculated by Legris and Domain [8] and Tu et al. [9]. Table 1 shows there is some variation in the formation energy of the two types of iodine defects considered in bulk zirconium but the values are relatively close in energy. Different DFT codes and parameters were used for the calculations.

The adsorption energy of an isolated iodine atom was also calculated in order to make comparisons. The adsorption energy was calculated to be -3.84 eV. The adsorption energy of a molecule, from literature [46], is approximately -6.2 eV per I_2 molecule or approximately -3.1 eV per atom.

3.2. Iodine Defects in Bulk Zirconium

The formation energy of an iodine octahedral interstitial defect at the two crack tip configurations from Figure 2 were 0.14 eV at a uniaxial tensile strain (ϵ_{yy}) of 0.05 and -2.49 eV at a uniaxial tensile strain of 0.16. As the tensile strain increased, the defect formation energy became more favourable. This is unsurprising given the relatively large atomic size of iodine. These results provided the motivation for further studying the effect of strain on the formation energies of iodine defects in zirconium.

Figure 8 shows the energies for iodine substitutional and interstitial formation energies in bulk HCP Zr and compares these energies to the adsorption energies of iodine on the [0001] Zr surface, as a function of strain. This comparison was made as it is a prevailing theory that iodine will remain on the surface of Zr as the adsorption energies are lower (more favourable) than the substitutional and interstitial energies in bulk Zr. Indeed, this latter part is true when considering a bare Zr surface.

8

However, calculations of the adsorption of iodine atoms on an oxygen terminated surface (replacing an oxygen) are comparatively less favourable. This is due to the fact that oxygen has a strong binding to the Zr surface. In fact, when comparing the substitutional and interstitial energies of iodine to the adsorption energy of iodine, in the presence of oxygen, it is the substitutional energy of iodine onto a Zr site that is the more favoured for all strains and even the interstitial iodine energy is more favoured between strains of 1-5% in tension. It is acknowledged that it is common practice for a diatomic iodine molecule to be used as a reference state for similar calculations. Although it is not clear what state iodine will be in during SCC scenarios, we have performed a comparison between an isolated iodine atom and diatomic iodine to quantify the difference of 1 eV in favourability. This difference does not change the relative favourabilities of the compared mechanisms. It is therefore plausible that iodine could exist in the bulk Zr matrix as a subsitutional defect, and additionally an interstitial defect in regions of tension i.e. at a crack tip of order of nanometres, as shown for iodine stress corrosion of Zr. At a cladding crack tip under reactor conditions, neutron irradiation damage will create other types of defects including self-interstitials and vacancies and the defect population will be higher than equilibrium levels. Kenich et al. [34] showed that iodine substitution onto Zr sites is likely to occur. Consequently, it is important to consider the case of an iodine atom occupying a zirconium vacancy and these defects are important for the diffusion of iodine in zirconium. It was observed that the hydrostatic strain did not have a significant effect on the formation energy of an iodine substitutional defect in pure Zr. For interstitial defects the space available increased significantly with increasing hydrostatic tensile strain. For substitutional defects, as the iodine took the place of a zirconium atom, the formation energy was not as affected by strain. In addition, any volumetric mismatch in the case of a substitutional defect is expected to be minimal.

Equations 5 and 6 were used to calculate the relative energies between a surface adsorbed iodine atom and unstrained bulk zirconium. The surface defect formation energy was 3.31 eV lower for the substitutional defect and 4.86 eV lower for the interstitial defect. It is noted that the formation energies of both interstitial and substitutional defects are higher than the adsorption of an iodine atom onto an unstrained oxygen free Zr surface. While the mechanism of iodine ingress into the bulk structure is not nvestigated here, its presence below the surface is observed in past literature [12, 13]. We assume here that the structures iodine will substitute into will be the sub-oxide layers, present just below the ruptured or porous oxide surface. Even if the oxide film is completely ruptured,

9

²²⁰ oxygen diffusion would likely prevent iodine from encountering an unstrained oxygen-free bulk-Zr surface through diffusion. Consequently, alternative mechanisms of iodine reaching zirconium metal should be considered and investigated including grain boundaries [47] and nano-pipes in strained structures [48].

3.3. Iodine Defects in Ordered Suboxides

²²⁵ Figure 9 shows the formation energies of iodine interstitial and substitutional defects in unstrained and 3 % strained bulk Zr and the structured suboxides considered. For ZrO, only the lowest energy site (ZrO-4) is shown with an iodine defect formation energy of 8.60 eV. The other sites (not shown), ZrO-1, ZrO-2 and ZrO-3 had even higher energies of 9.3, 11.5 and 13.6 eV respectively. As the oxygen content of the structures increased, the formation energies of the interstitial ²³⁰ defects increased from 1.03 eV in pure zirconium to 8.60 eV in ZrO. It is worth noting that these defect formation energies are very high and unlikely to occur under normal conditions. The increase from Zr to Zr_2O was relatively linear (given the approximately equal increase in oxygen concentrations) followed by a larger jump in energy to ZrO as the oxygen content increased significantly. The higher iodine interstitial defect formation energies in the structures with higher oxygen concentrations support the idea that oxygen has a protective effect against iodine ingress at the crack tip. How these energies compare to the adsorption energies of iodine to the respective sub-oxide surfaces has not been quantified to-date and was not within the scope of this work.

A pristine zirconium cladding has an oxide layer of ZrO_2 and below this layer, as the distance from the cladding surface increases inwards, structures with decreasing oxygen content are found [22, ²⁴⁰ 29, 30, 31, 32, 33]. In work studying defect concentrations in the oxide layer, Kenich et al. [34] showed that in the monoclinic phase iodine occupied oxygen anion sites with an oxidation state of -1. In the tetragonal phase at high oxygen partial pressures iodine defects preferred zirconium cation sites instead of anion sites suggesting the oxygen has a blocking effect on iodine defect formation. Figure 9 (top) shows that as the oxygen content decreases, the competition between ²⁴⁵ oxygen and iodine becomes less significant as reflected by the lower formation energy of iodine defects. Nonetheless, a 3 % hydrostatic tensile strain was found to simultaneously decrease the energy of formation of iodine interstitial defects more in structures with increasing oxygen content. Although the oxide layer's protective effect against I-SCC has been shown, it was suggested that it must remain intact in order to fulfill that role [49] negating the role of oxygen in the underlying

10

metal. The oxide was postulated to have to partially break and expose the metal surface underneath in order for I-SCC to be possible [3, 50, 51]. Videm and Lunde [18] made a similar observation for Zircaloy at 340 °C. For unstrained and unstressed specimens, I_2 did not react for days or even weeks. At the same time, Hu et al. [48] showed that diffusion of H, albeit the smallest of atoms, can occur through nanopores in the corrosion film layer and can then diffuse through nano-pipes and reach the suboxide layers. Figure 9 (bottom) shows the magnitude of the energy decrease between the formation energy of the interstitial defect in the unstrained and the 3 % tensile strained structures. In pure zirconium, a 3 % hydrostatic tensile strain caused the iodine interstitial formation energy to decrease by 1.47 eV to -0.44 eV.In ZrO, applying a 3 % hydrostatic tensile strain caused the formation energy to decrease by 4.56 eV, a much larger decrease than the 1.47 eV for pure zirconium. Nonetheless, it still has a large positive energy of 4.04 eV. The findings suggest that in a highly tensile strained structure the oxygen might actually lead to more defect incorporation possibly due to the oxygen causing the lattice to expand while leaving enough interstitial sites available for iodine [48]. The existence of nanopores can allow chemical species to diffuse through. Combining the diffusion mechanism for iodine diffusion in zirconium investigated by Tu et al. [9] with the existence of irradiation induced vacancies and a strained lattice could provide a path for the iodine to diffuse through to the suboxides. The larger decrease in iodine interstitial defect formation energies with increasing oxygen could account for the the occurrence of I-SCC in the presence of a strained or damaged oxide.

An increase in formation energy was also exhibited by iodine substitutional defects in the structured suboxides as the oxygen content increased. The substitutional iodine defect formation energy was also lower than the interstitial iodine defect energy reflecting the same trend that was observed for iodine defects in pure zirconium (Figure 8 in Section 3.2). The effect of strain on substitutional defects, however, wasn't as significant as it was for interstitial defects. Kenich et al. [34] showed that as the oxygen partial pressure increased in ZrO_2, the iodine defects would preferentially form on Zr sites. In the current work, as oxygen content increased and tensile strain was applied, the interstitial defect formation energy was very similar to the unstrained zirconium substitutional defect formation energy and was even lower than the substitutional defect for some of the structures and sites considered as seen in Figure 9. For Zr_3O, the formation energy of an iodine interstitial defect under 3 % tensile hydrostatic strain was 1.24 eV compared to the 1.45 eV formation energy for an unstrained iodine substitutional defect. Similarly, it was lower for the Zr_2O-1 site as well: 1.91 eV

11

vs. 2.21 eV. Nonetheless, the substitutional defect formation energy in the 3 % strained structures was always lower than the interstitial defect formation energies. Substitutional defects are likely to form preferentially (0.1–1.5 eV lower depending on the structure) to interstitial defects for the strain considered in this work but for higher than 3 % strains, as shown at crack tips in Figures 1 and 2, that may not be true.

3.4. Bond Population and Length Analysis

The bond population for the Zr-I bonds in both the unstrained and strained structures is shown in Figure 10a. Please note that all the bond population values shown are the averages of the respective bonds. As the oxygen content increased the bond population value became more negative suggesting the interaction was increasingly antibonding. Figure 10b shows the percentage increase in the Zr-I bond length for all the structures due to the 3 % hydrostatic tensile strain applied compared to the unstrained structure. For bulk zirconium there was a 1.6 % increase whereas for ZrO the bond length increased by 6.0 %. In a structure devoid of oxygen, the large electronegativity of iodine keeps the surrounding zirconium atoms close to it, even when strain was applied. For ZrO, however, a more detailed analysis is needed. Figure 11 shows the Mulliken charges for the 1st neighbouring Zr atoms (average), the I atom and the 1st neighbouring O atoms (average). For ZrO, the Mulliken charge on the Zr atoms for the defect free structure was slightly lower when strain was applied. For the other structures the difference was insignificant. The high electronegativity of oxygen causes a strong attraction for the electron density available. When strain was applied, however, that attraction was weakened more than for the other structures. As a result, the bond length increase was higher when the tensile hydrostatic strain was applied. Consequently, the decrease in the defect formation energy due to strain was larger for ZrO than it was for Zr.

Figure 11 also shows that as the oxygen content increased, the charge on the Zr atoms became more positive. The highly electronegative oxygen pulls more of the electron density (becoming more negative in the process, especially in ZrO as seen in Figure 11c) and the Zr atoms become increasingly positively charged. Consequently, the structure loses some of its metallic nature.

Figures 12 and 13 show the bond population and bond length values for the Zr-Zr and Zr-O bonds. For both the I-bonded and the non I-bonded Zr-Zr bonds, the bond population decreased from a value of approximately 0.2 to close to 0. A higher positive value implies the structure has a more metallic nature (electron sharing), whereas a value closer to 0 implies the structure has a

12

more ionic character. As the oxygen content increased, the ionic nature of the Zr-Zr bonds also increased and the structure showed a less metallic nature. Point defects (such as interstitial defects) in ceramic materials are charged. Consequently, introducing an interstitial defect in an increasingly ionic-like material would lead to a greater charge imbalance. The increasing Coulombic forces cause the formation energy of the defect to increase. Therefore, as the oxygen content was increased the formation energy of an iodine interstitial defect also increased (seen in Figure 9). It is also noted that the DFT calculations of all the suboxide structures indicated a metallic nature that decreased as the oxygen content increased as shown in Figure 14. This included ZrO although there is a clear decrease in states at the Fermi level compared to structures with less oxygen. Nonetheless, Annand et al. [23] used a dual electron energy loss spectroscopy (DualEELS) technique to show that the ZrO phase is no longer metallic in nature, but is either an insulator or more likely a semiconductor. As the current work used a GGA approach it is not surprising that it may underpredict the band gap. The defect formation energy is likely to be higher than the value calculated in Section 3.3 and the bond population value to be lower due to an even more ionic nature of the structure than that indicated by the DFT calculations.

For the non I-bonded Zr-Zr bonds, there was little difference between the structures with an iodine interstitial defect and the defect free structures. The larger distance between the atoms involved in those bonds and the iodine defect prevented the iodine defect from having a significant impact on the bonding. The strain did, however, have a noticeable effect. For all oxygen contents (all structures), the Zr-Zr bond populations in the strained structures were higher than in the unstrained ones. The increase in bond population values for all Zr-Zr bonds due to strain was approximately the same for all the structures. In addition, the Zr-Zr bond length also increased with higher oxygen content. Although the increase in the ionic nature of the structure, due to increasing oxygen content, caused the iodine interstitial defect formation energies to increase, an applied tensile strain did the opposite, allowing the structure to retain more of its metallic nature and thus causing the defect formation energy to decrease relative to the unstrained case (see Figure 9).

Figures 12 and 13 also show the bond population and length values for the Zr-O bonds in both the 3 % hydrostatically tensile strained and unstrained structures. For the non I-bonded atoms, just like for the non I-bonded Zr-Zr bonds, the presence of the defect did not have a significant impact on the bond populations or bond lengths. The Zr-O bond length also increased with higher oxygen content. As more oxygen was present in the lattice, the structure expanded in order to be

able to accommodate it. The oxygen content did not have a significant impact on the Zr-O bond population values. The tensile strain did, however, have the same effect as on the non I-bonded Zr-Zr bonds. The tensile strain resulted in the structure having a more metallic nature. Consequently, an applied hydrostatic strain would lead to easier defect incorporation into the structure.

For the I-bonded Zr-O bonds, the oxygen content and incorporation of an iodine interstitial defect did affect structures differently to some extent. Overall, the Zr-O bond length increased as the oxygen content increased. The bond population also stayed relatively constant save for the Zr_6O-2 and Zr_2O-1 structures. The incorporation of the iodine defect led to a significant increase in the Zr-O bond population values in the Zr_6O-2 site but not Zr_6O-1 or Zr_6O-3. In both the Zr_6O-1 or Zr_6O-3 sites, the iodine interstitial defect is closer to the existing oxygen atoms (3 Å for Zr_6O-1 and 3.4 Å for Zr_6O-3 compared to >4 Å for Zr_6O-2). As a result, not only were the defect formation energies higher (3.0 and 2.6 eV compared to 2.4 eV for Zr_6O-2), the electron density pull by the iodine is weaker for both structures. In the Zr_6O-2 site, because the iodine was further away from any oxygen atoms, it pulled more of the available electron density from the surrounding zirconium atoms. Figure 11 shows that the charge on the I atom in the Zr_6O-2 structure is less positive than the charges on the I atom in the Zr_6O-1 or Zr_6O-3 structures. That increase in electron density can also be seen in Figure 15 where the PDOS for iodine has a more pronounced peak at an energy of approximately 3 eV. Consequently, the zirconium atoms were then pulled closer towards the oxygen atoms and the Zr-O bond length was shorter. At the same time, the bond population was higher indicating a more metallic local bonding in the structure. The same behaviour was seen for the Zr_2O structures. In the Zr_2O-2 site, the iodine defect is surrounded by more oxygen atoms (8 different atoms) than in Zr_2O-1 (2 atoms). Consequently, the charge on the iodine atom is higher in Zr_2O-2 than it is in Zr_2O-1 (as seen in Figure 11). The proximity of the iodine defect to the nearest oxygen atoms in the structure impacts the formation energy of the defect even in structures that have the same overall amount of oxygen. Understanding how each of the structures affects the various processes occurring during I-SCC (such as diffusion) is therefore essential in order to build a complete mechanistic understanding of I-SCC. The diffusion process via interstitial sites in bulk zirconium [9] will be affected by increasing oxygen content in the various structured suboxides and is likely to be favoured by increased tensile hydrostatic strain similar to the strain states envisaged at very sharp crack tips.

14

4. Conclusions

1. considering an oxygen terminated [0001] Zr surface, the adsorption energy (replacement of oxygen ion) is energetically less favourable than the substitution of a bulk Zr atom with iodine for all strains investigated.

2. The formation energy of a single iodine octahedral interstitial defect in bulk zirconium was found to decrease with increasing hydrostatic strain whereas the substitutional defect formation energy and [0001] surface adsorption energies were relatively unaffected by strain.

3. In unstrained structures, the iodine octahedral interstitial defect formation energy increased (less favourable) with increasing oxygen content supporting the oxygen's protective role at a crack tip in the presence of iodine.

4. A 3 % hydrostatic tensile strain was found to decrease the energy of formation of iodine interstitial defects more in structures with higher oxygen content.

5. Substitutional iodine defects would likely form preferentially to octahedral interstitial defects at zero strain but tensile strain significantly narrows the gap between them possibly even reversing the trend for very large (>5 %) strains possible at an SCC tip.

15

Data Availability

The raw/processed data required to reproduce these findings cannot be shared at this time due to technical or time limitations but will be available upon request.

References

[1] M. Frégonèse, G. Delette, G. Ducros, F. Lefebvre, Amount of iodine responsible for I-SCC of Zircaloy-4 in PCI-conditions: recoil-implanted and thermally released iodine, Nuclear Engineering and Design 186 (3) (1998) 307–322. `doi:10.1016/S0029-5493(98)00289-1`.

[2] P. S. Sidky, Iodine stress corrosion cracking of Zircaloy reactor cladding: iodine chemistry (a review), Journal of Nuclear Materials 256 (1) (1998) 1–17. `doi:10.1016/S0022-3115(98)00044-0`.
URL `http://linkinghub.elsevier.com/retrieve/pii/S0022311598000440`

[3] B. J. Lewis, W. T. Thompson, M. R. Kleczek, K. Shaheen, M. Juhas, F. C. Iglesias, Modelling of iodine-induced stress corrosion cracking in CANDU fuel, Journal of Nuclear Materials 408 (3) (2011) 209–223. `doi:10.1016/j.jnucmat.2010.10.063`.
URL `http://dx.doi.org/10.1016/j.jnucmat.2010.10.063`

[4] W. T. Grubb, M. H. Morgan, A Survey of the Chemical Environments for Activity in the Embrittlement of Zircaloy-2, in: J. H. Schemel, T. P. Papazoglou (Eds.), Zirconium in the Nuclear Industry, Proceedings of the Fourth International Conference, ASTM STP681, ASTM International, Stratford-upon-Avon, England, 1979, pp. 145–154. `doi:10.1520/STP36677S`.
URL `http://www.astm.org/doiLink.cgi?STP36677S`

[5] B. Cox, Environmentally-induced cracking of zirconium alloys — A review, Journal of Nuclear Materials 170 (1) (1990) 1–23. `doi:10.1016/0022-3115(90)90321-D`.
URL `http://linkinghub.elsevier.com/retrieve/pii/002231159090321D`

[6] M. L. Rossi, C. D. Taylor, First-principles insights into the nature of zirconium-iodine interactions and the initiation of iodine-induced stress-corrosion cracking, Journal of Nuclear Materials 458 (2015) 1–10. `doi:10.1016/j.jnucmat.2014.11.114`.
URL `http://dx.doi.org/10.1016/j.jnucmat.2014.11.114`

16

[7] J. C. Wood, Factors affecting stress corrosion cracking of zircaloy in iodine vapour, Journal of Nuclear Materials 45 (2) (1972) 105–122. `doi:10.1016/0022-3115(72)90178-X`.
URL `http://linkinghub.elsevier.com/retrieve/pii/002231157290178X`

[8] A. Legris, C. Domain, Ab initio atomic-scale modelling of iodine effects on hcp zirconium, Philosophical Magazine 85 (4-7) (2005) 589–595. `doi:10.1080/02678370412331320099`.
URL `http://www.informaworld.com/openurl?genre=article%7B%5C&%7Ddoi=10.1080/02678370412331320099%7B%5C&%7Dmagic=crossref%7B%5C%25%7D7C%7B%5C%25%7D7CD404A21C5BB053405B1A640AFFD44AE3`

[9] R. Tu, Q. Liu, C. Zeng, Y. Li, W. Xiao, First principles study of point defect effects on iodine diffusion in zirconium, Nuclear Materials and Energy 16 (July) (2018) 238–244. `doi:10.1016/j.nme.2018.07.006`.
URL `https://linkinghub.elsevier.com/retrieve/pii/S2352179118300413`

[10] L. Liu, R. Tu, L. Chu, Y. Li, C. Sun, D. Shao, W. Xiao, First-principles study for strain effects on oxygen migration in zirconium, Computational Materials Science 144 (2018) 345–354. `doi:10.1016/j.commatsci.2017.12.051`.
URL `https://doi.org/10.1016/j.commatsci.2017.12.051`

[11] C. D. Taylor, M. L. Rossi, Multiphysics Modeling of the Role of Iodine in Environmentally Assisted Cracking of Zirconium via Pellet-Clad Interaction, Corrosion 72 (7) (2016) 978–988. `doi:10.5006/1923`.
URL `http://corrosionjournal.org/doi/10.5006/1923`

[12] C. Gillen, A. Garner, A. Plowman, C. P. Race, T. Lowe, C. Jones, K. L. Moore, P. Frankel, Advanced 3D characterisation of iodine induced stress corrosion cracks in zirconium alloys, Materials Characterization 141 (January 2018) (2018) 348–361. `doi:10.1016/j.matchar.2018.04.034`.
URL `https://doi.org/10.1016/j.matchar.2018.04.034https://linkinghub.elsevier.com/retrieve/pii/S1044580318300263`

[13] C. Gillen, A. Garner, P. Tejland, P. Frankel, High resolution crystallographic and chemical characterisation of iodine induced stress corrosion crack tips formed in irradiated and non-irradiated zirconium alloys, Journal of Nuclear Materials 519 (2019) 166–172. `doi:10.1016/`

17

j.jnucmat.2019.03.027.

URL https://doi.org/10.1016/j.jnucmat.2019.03.027

[14] L. Brunisholz, C. Lemaignan, Iodine-Induced Stress Corrosion of Zircaloy Fuel Cladding: Initiation and Growth, in: R. B. Adamson, L. F. P. Van Swam (Eds.), Zirconium in the Nuclear Industry, Proceedings of the Seventh International Conference, ASTM STP939, ASTM International, Strasbourg, France, 1987, pp. 700–716. doi:10.1520/STP28154S.

URL http://www.astm.org/doiLink.cgi?STP28154S

[15] K. Une, Stress Corrosion Cracking of Zircaloy-2 Cladding in Iodine Vapor, Journal of Nuclear Science and Technology 14 (6) (1977) 443–451. doi:10.1080/18811248.1977.9730783.

URL http://www.tandfonline.com/doi/abs/10.1080/18811248.1977.9730783

[16] D. Cubicciotti, R. L. Jones, B. C. Syrett, Chemical Aspects of Iodine-Induced Stress Corrosion Cracking of Zircaloys, in: D. G. Franklin (Ed.), Zirconium in the Nuclear Industry, Proceedings of the Fifth International Conference, ASTM STP754, ASTM International, Boston, MA, 1982, pp. 146–157. doi:10.1520/STP37052S.

URL http://www.astm.org/doiLink.cgi?STP37052S

[17] L. F. Coffin, Localized Ductility Method for Evaluating Zircaloy-2 Cladding, in: J. H. Schemel, T. P. Papazoglou (Eds.), Zirconium in the Nuclear Industry, Proceedings of the Fourth International Conference, ASTM STP681, ASTM International, Stratford-upon-Avon, England, 1979, pp. 72–87. doi:10.1520/STP36673S.

URL http://www.astm.org/doiLink.cgi?STP36673S

[18] K. Videm, L. Lunde, Stress Corrosion Crack Initiation and Growth and Formation of Pellet-Clad Interaction Defects, in: J. H. Schemel, T. P. Papazoglou (Eds.), Zirconium in the Nuclear Industry, Proceedings of the Fourth International Conference, ASTM STP681, ASTM International, Stratford-upon-Avon, England, 1979, pp. 229–243. doi:10.1520/STP36683S.

URL http://www.astm.org/doiLink.cgi?STP36683S

[19] Y. Tsing-Tyan, T. Chuen-Horng, On the susceptibility to stress corrosion cracking of Zircaloy in an iodine containing environment, Journal of Nuclear Materials 166 (3) (1989) 252–264. doi:10.1016/0022-3115(89)90222-5.

URL http://linkinghub.elsevier.com/retrieve/pii/0022311589902225

18

[20] B. Cox, The effect of surface films on the initiation of stress corrosion cracking of Zircaloy-2. Report Number AECL-4589, Tech. Rep. June, Chalk River Nuclear Laboratories, Chalk River, Ontario, Canada (1973).
URL `http://www.iaea.org/inis/collection/NCLCollectionStore/%7B%5C_%7DPublic/04/088/4088097.pdf`

[21] R. F. Mattas, F. L. Yaggee, L. A. Neimark, Effect of Zirconium Oxide on the Stress-Corrosion Susceptibility of Irradiated Zircaloy Cladding, in: D. G. Franklin (Ed.), Zirconium in the Nuclear Industry, Proceedings of the Fifth International Conference, ASTM STP754, ASTM International, Boston, MA, 1982, pp. 158–170. `doi:10.1520/STP37053S`.
URL `http://www.astm.org/doiLink.cgi?STP37053S`

[22] J. Hu, A. Garner, N. Ni, A. Gholinia, R. J. Nicholls, S. Lozano-Perez, P. Frankel, M. Preuss, C. R. M. Grovenor, Identifying suboxide grains at the metal–oxide interface of a corroded Zr–1.0%Nb alloy using (S)TEM, transmission-EBSD and EELS, Micron 69 (2015) 35–42. `doi:10.1016/j.micron.2014.10.004`.
URL `http://linkinghub.elsevier.com/retrieve/pii/S0968432814001887`

[23] K. J. Annand, I. MacLaren, M. Gass, Utilising DualEELS to probe the nanoscale mechanisms of the corrosion of Zircaloy-4 in 350 °C pressurised water, Journal of Nuclear Materials 465 (2015) 390–399. `doi:10.1016/j.jnucmat.2015.06.022`.
URL `http://dx.doi.org/10.1016/j.jnucmat.2015.06.022https://linkinghub.elsevier.com/retrieve/pii/S0022311515300477`

[24] T.-W. Chiang, A. Chernatynskiy, M. J. Noordhoek, S. B. Sinnott, S. R. Phillpot, Anisotropy in oxidation of zirconium surfaces from density functional theory calculations, Computational Materials Science 98 (2015) 112–116. `doi:10.1016/j.commatsci.2014.10.052`.
URL `http://dx.doi.org/10.1016/j.commatsci.2014.10.052http://linkinghub.elsevier.com/retrieve/pii/S0927025614007502https://linkinghub.elsevier.com/retrieve/pii/S0927025614007502`

[25] B. J. Flinn, C.-S. Zhang, P. R. Norton, Oxygen diffusion along the [0001] axis in Zr(0001), Physical Review B 47 (24) (1993) 16499–16505. `doi:10.1103/PhysRevB.47.16499`.
URL `https://link.aps.org/doi/10.1103/PhysRevB.47.16499`

19

[26] G. M. Hood, Point defect diffusion in α-Zr, Journal of Nuclear Materials 159 (C) (1988) 149–175. doi:10.1016/0022-3115(88)90091-8.
URL http://linkinghub.elsevier.com/retrieve/pii/0022311588900918

[27] G. M. Hood, H. Zou, S. Herbert, R. J. Schultz, H. Nakajima, J. A. Jackman, Oxygen diffusion in α-Zr single crystals, Journal of Nuclear Materials 210 (1-2) (1994) 1–5. doi:10.1016/0022-3115(94)90215-1.
URL https://linkinghub.elsevier.com/retrieve/pii/0022311594902151

[28] I. G. Ritchie, A. Atrens, The diffusion of oxygen in alpha-zirconium, Journal of Nuclear Materials 67 (3) (1977) 254–264. doi:10.1016/0022-3115(77)90097-6.
URL https://linkinghub.elsevier.com/retrieve/pii/0022311577900976

[29] R. J. Nicholls, N. Ni, S. Lozano-Perez, A. London, D. W. McComb, P. D. Nellist, C. R. M. Grovenor, C. J. Pickard, J. R. Yates, Crystal structure of the ZrO phase at zirconium/zirconium oxide interfaces, Advanced Engineering Materials 17 (2) (2015) 211–215. doi:10.1002/adem.201400133.

[30] B. Puchala, A. Van der Ven, Thermodynamics of the Zr-O system from first-principles calculations, Physical Review B 88 (9) (2013) 94108. doi:10.1103/PhysRevB.88.094108.
URL https://link.aps.org/doi/10.1103/PhysRevB.88.094108

[31] J. Zhang, A. R. Oganov, X. Li, H. Dong, Q. Zeng, Novel compounds in the Zr–O system, their crystal structures and mechanical properties, Physical Chemistry Chemical Physics 17 (26) (2015) 17301–17310. doi:10.1039/C5CP02252E.
URL http://dx.doi.org/10.1039/C5CP02252E

[32] T. Ericsson, G. Östberg, B. Lehtinen, Some observations on Zr-O solid solutions with a microprobe and by electron microscopy, Journal of Nuclear Materials 25 (3) (1968) 322–327. doi:10.1016/0022-3115(68)90177-3.
URL https://linkinghub.elsevier.com/retrieve/pii/0022311568901773

[33] A. Yilmazbayhan, E. Breval, A. T. Motta, R. J. Comstock, Transmission electron microscopy examination of oxide layers formed on Zr alloys, Journal of Nuclear Materials 349 (3) (2006) 265–281. doi:10.1016/j.jnucmat.2005.10.012.
URL https://linkinghub.elsevier.com/retrieve/pii/S0022311505005106

20

[34] A. Kenich, M. R. Wenman, R. W. Grimes, Iodine defect energies and equilibria in ZrO2, Journal of Nuclear Materials 511 (2018) 390–395. `doi:10.1016/j.jnucmat.2018.09.018`.

[35] F. Bianchini, J. R. Kermode, A. De Vita, Modelling defects in Ni–Al with EAM and DFT calculations, Modelling and Simulation in Materials Science and Engineering 24 (4) (2016) 45012. `doi:10.1088/0965-0393/24/4/045012`.
URL `http://stacks.iop.org/0965-0393/24/i=4/a=045012?key=crossref.ddf95138bfc65412b6de59dcee26df6c`

[36] Z. Li, J. R. Kermode, A. De Vita, Molecular Dynamics with On-the-Fly Machine Learning of Quantum-Mechanical Forces, Physical Review Letters 114 (9) (2015) 96405. `doi:10.1103/PhysRevLett.114.096405`.
URL `https://link.aps.org/doi/10.1103/PhysRevLett.114.096405`

[37] S. J. Clark, M. D. Segall, C. J. Pickard, P. J. Hasnip, M. I. J. Probert, K. Refson, M. C. Payne, First principles methods using CASTEP, Zeitschrift für Kristallographie 220 (5/6/2005) (2005) 567–570.

[38] F.-H. Wang, S.-Y. Liu, J.-X. Shang, Y.-S. Zhou, Z. Li, J. Yang, Oxygen adsorption on Zr(0001) surfaces: Density functional calculations and a multiple-layer adsorption model, Surface Science 602 (13) (2008) 2212–2216. `doi:10.1016/j.susc.2008.04.033`.
URL `https://linkinghub.elsevier.com/retrieve/pii/S0039602808002926`

[39] X. Wang, M. Khafizov, I. Szlufarska, Effect of surface strain on oxygen adsorption on Zr (0001) surface, Journal of Nuclear Materials 445 (1-3) (2014) 1–6. `doi:10.1016/j.jnucmat.2013.10.046`.
URL `http://dx.doi.org/10.1016/j.jnucmat.2013.10.046https://linkinghub.elsevier.com/retrieve/pii/S0022311513011963`

[40] L. Zhang, J. Jasa, G. Gazonas, A. Jérusalem, M. Negahban, Extracting continuum-like deformation and stress from molecular dynamics simulations, Computer Methods in Applied Mechanics and Engineering 283 (2015) 1010–1031. `doi:10.1016/j.cma.2014.10.018`.

[41] J. Zhang, A. R. Oganov, X. Li, M. Mahdi Davari Esfahani, H. Dong, First-principles investigation of Zr-O compounds, their crystal structures, and mechanical properties, Journal of

21

Applied Physics 121 (15) (2017). `doi:10.1063/1.4979913`.

570   URL `http://dx.doi.org/10.1063/1.4979913`

[42] D. Sanchez-Portal, E. Artacho, J. M. Soler, Projection of plane-wave calculations into atomic orbitals, Solid State Communications 95 (10) (1995) 685–690. `arXiv:9505075`, `doi:10.1016/0038-1098(95)00341-X`.

[43] R. S. Mulliken, Electronic Population Analysis on LCAO, J. Chem. Phys 23 (December) (1955) 575   1833.

[44] M. D. Segall, C. J. Pickard, R. Shah, M. C. Payne, Population analysis in plane wave electronic structure calculations, Molecular Physics 89 (2) (1996) 571–577. `doi:10.1080/002689796173912`.
URL   `http://www.tandfonline.com/doi/full/10.1080/002689796173912http:` 580   `//www.epa.gov/air/basic.html`

[45] R. Han, L. Liu, R. Tu, W. Xiao, Y. Li, H. Li, D. Shao, Iodine Atom Diffusion in SiC and Zirconium with First-Principles Calculations, Nuclear Technology 195 (2) (2016) 192–203. `doi:http://dx.doi.org/10.13182/NT15-109`.
URL `https://www.tandfonline.com/doi/full/10.13182/NT15-109`

585 [46] E. Wimmer, R. Najafabadi, G. A. Young Jr, J. D. Ballard, T. M. Angeliu, J. Vollmer, J. J. Chambers, H. Niimi, J. B. Shaw, C. Freeman, M. Christensen, W. Wolf, P. Saxe, Ab initio calculations for industrial materials engineering: successes and challenges, Journal of Physics: Condensed Matter 22 (38) (2010) 384215. `doi:10.1088/0953-8984/22/38/384215`.
URL `https://iopscience.iop.org/article/10.1088/0953-8984/22/38/384215`

590 [47] A. J. Plowman, Developing a mechanistic understanding of the pellet-cladding interaction with atomistic simulation, Ph.D. thesis, University of Manchester (2018).
URL `https://ethos.bl.uk/OrderDetails.do?uin=uk.bl.ethos.771519`

[48] J. Hu, J. Liu, S. Lozano-Perez, C. R. M. Grovenor, M. Christensen, W. Wolf, E. Wimmer, E. V. Mader, Hydrogen pickup during oxidation in aqueous environments: The role 595   of nano-pores and nano-pipes in zirconium oxide films, Acta Materialia 180 (2019) 105–115. `doi:10.1016/j.actamat.2019.09.005`.

22

URL `https://doi.org/10.1016/j.actamat.2019.09.005https://linkinghub.elsevier.com/retrieve/pii/S1359645419305853`

[49] D. Cubicciotti, S. M. Howard, R. L. Jones, The formation of iodine-induced stress corrosion cracks in zircaloys, Journal of Nuclear Materials 78 (1) (1978) 2–16. `doi:10.1016/0022-3115(78)90498-1`.
URL `http://linkinghub.elsevier.com/retrieve/pii/0022311578904981`

[50] P. Hofmann, J. Spino, Determination of the critical iodine concentration for stress corrosion cracking failure of Zircaloy-4 tubing between 500 and 900°C, Journal of Nuclear Materials 107 (2-3) (1982) 297–310. `doi:10.1016/0022-3115(82)90429-9`.
URL `http://linkinghub.elsevier.com/retrieve/pii/0022311582904299`

[51] M. Nagai, S. Shimada, S. Nishimura, K. Amano, Elucidating the Iodine Stress Corrosion Cracking (SCC) Process for Zircaloy Tubing, in: Proceedings of a Specialists' Meeting on Pellet Cladding Interaction in Water Reactor Fuel., IAEA, Seattle, USA, 1983, pp. 89–102.
URL `https://inis.iaea.org/search/search.aspx?orig%7B%5C_%7Dq=RN:16050711`

23

Figure Captions

1. Crack tip extracted from a pure zirconium slab subject to a strain equivalent to a G (energy release rate) value of 3.0 J m^{-2}. The strains shown are in the y-direction (ϵ_{yy}) [0001] and in the x-direction (ϵ_{xx}) [1$\bar{2}$10]. Due to the plane-strain nature of the model the strains in the z-direction (ϵ_{zz}) [$\bar{1}$010] were approximately zero. The minimum value of ϵ_{yy} represents the strain the entire slab was subject to in order to create the edge crack. Only the top layer of atoms is shown for clarity.

2. Octahedral interstitial positions for iodine (red) at a strained crack tip configuration extracted from a pure zirconium slab (green) subject to a strain equivalent to 3.0 J m^{-2}. There are 2 layers of atoms in the [$\bar{1}$010] direction repeated periodically. Only atoms from the full QM region where DFT was applied are shown.

3. (a) Zr$_6$O structure and (b-d) the three unique octahedral interstitial positions available in the Zr$_6$O structure (Zr$_6$O-1, Zr$_6$O-2 and Zr$_6$O-3 respectively).

4. (a) Zr$_3$O structure and (b) the single unique octahedral interstitial position available in the Zr$_3$O structure.

5. (a) Zr$_2$O structure and (b-c) the two unique octahedral interstitial positions available in the Zr$_2$O structure (Zr$_2$O-1 and Zr$_2$O-2).

6. (a) ZrO structure and (b-e) the four unique interstitial positions available in the ZrO structure (ZrO-1, ZrO-2, ZrO-3 and ZrO-4 respectively).

7. Illustration of the atoms analysed in the bond population analysis performed: bonds that contain at least an atom in the first shell around the iodine defect are termed *I-bonded* and colored purple and the rest are termed *non I-bonded*.

8. Formation energy of a single iodine octahedral interstitial or substitutional defect in pure zirconium as a function of hydrostatic strain (left panel) and comparison to I, O and O+I adsorption energies (right panel).

9. (top) Formation energies of the lowest energy iodine interstitial and substitutional defect in both unstrained and 3 % hydrostatic tensile strained zirconium, Zr$_6$O, Zr$_3$O, Zr$_2$O and ZrO. (bottom) The magnitude of the decrease in iodine interstitial defect formation energy due to the 3 % applied hydrostatic tensile strain ($E_{strained} - E_{unstrained}$).

10. (a) Zr-I bond population analysis and (b) Zr-I bond length analysis for unstrained and 3 % hydrostatically tensile strained structures for iodine in interstitial sites.

11. Mulliken charges for the 1st neighbouring Zr atoms (average), I atom and 1st neighbouring O atoms (average) in each of the structures.

12. Zr-Zr and Zr-O bond population analysis for unstrained and 3 % hydrostatically tensile strained structures for a single iodine interstitial defect.

13. Zr-Zr and Zr-O bond length analysis for unstrained and 3 % hydrostatically tensile strained structures for a single iodine interstitial defect.

14. Density of states for bulk Zr, Zr$_6$O, Zr$_3$O, Zr$_2$O and ZrO showing highest density of states, around the Fermi level, for Zr and progressively less states as oxygen content increases.

15. PDOS for the iodine interstitial atom in the 3 % tensile hydrostatic strained Zr$_6$O in the three positions labelled Zr$_6$O-1, Zr$_6$O-2 and Zr$_6$O-3.

Tables

Table 1: Iodine defect formation energies

Source	Octahedral Interstitial	Tetrahedral Interstitial	Zirconium Substitutional
VASP, GGA-PW, 36 Zr atoms, 225 eV cutoff energy [8]	0.78	—	-0.75
VASP, GGA-PBE, 216 Zr atoms, 350 eV cutoff energy [9]	1.21	1.01	-0.73
VASP, GGA-PBE, 64 Zr atoms, 176 eV cutoff energy [45]	1.32	—	—
Here: CASTEP, GGA-PBE, 150 Zr atoms, 400 eV cutoff energy	1.03	1.28	-0.56

Figure Captions
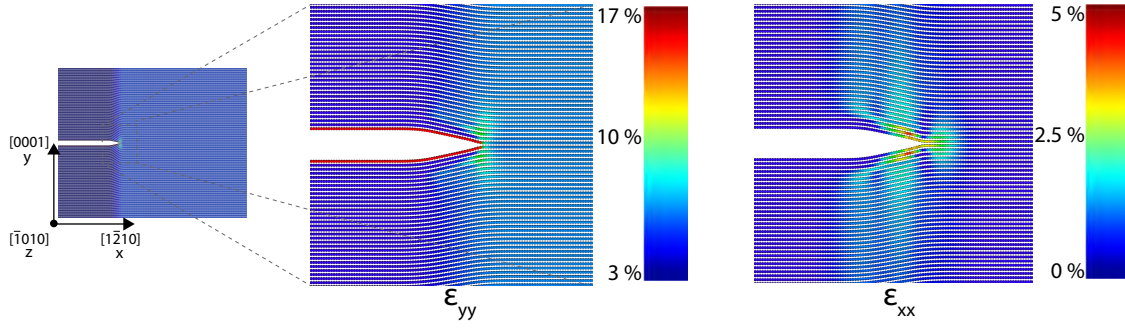
Figure 1: Crack tip extracted from a pure zirconium slab subject to a strain equivalent to a G (energy release rate) value of 3.0 J m^{-2}. The strains shown are in the y-direction (ϵ_{yy}) [0001] and in the x-direction (ϵ_{xx}) [1$\bar{2}$10]. Due to the plane-strain nature of the model the strains in the z-direction (ϵ_{zz}) [$\bar{1}$010] were approximately zero. The minimum value of ϵ_{yy} represents the strain the entire slab was subject to in order to create the edge crack. Only the top layer of atoms is shown for clarity.
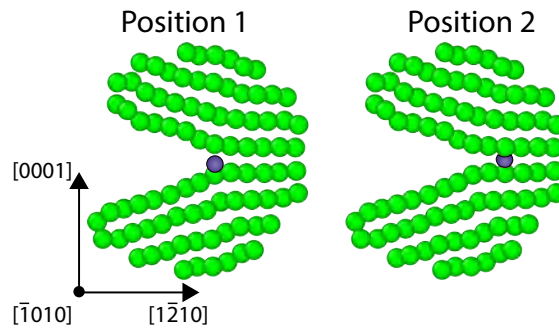
Figure 2: Octahedral interstitial positions for iodine (red) at a strained crack tip configuration extracted from a pure zirconium slab (green) subject to a strain equivalent to 3.0 J m^{-2}. There are 2 layers of atoms in the [$\bar{1}$010] direction repeated periodically. Only atoms from the full QM region where DFT was applied are shown.
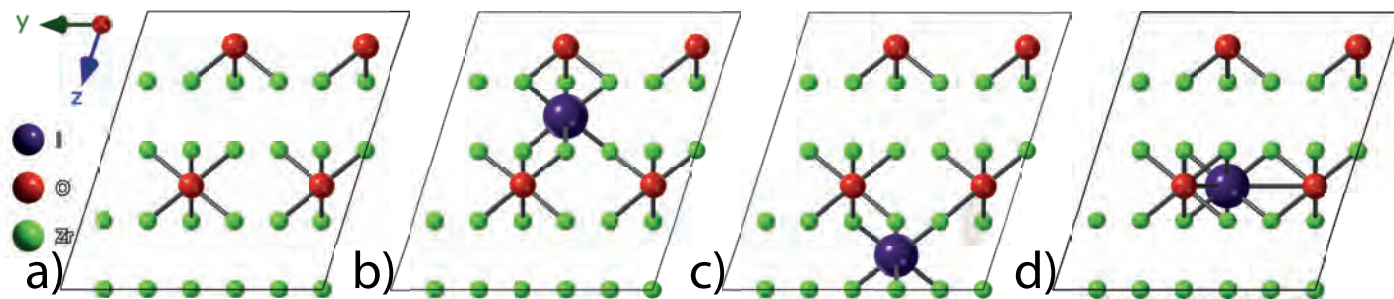
Figure 3: (a) Zr_6O structure and (b-d) the three unique octahedral interstitial positions available in the Zr_6O structure (Zr_6O-1, Zr_6O-2 and Zr_6O-3 respectively).
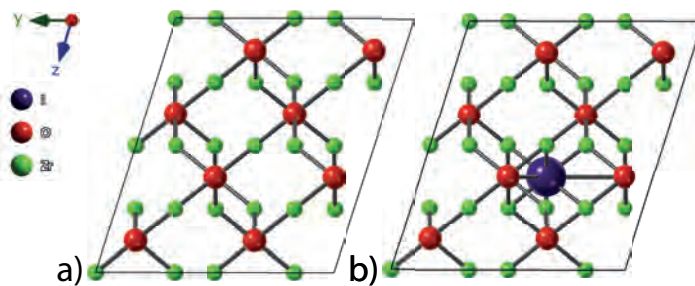
Figure 4: (a) Zr_3O structure and (b) the single unique octahedral interstitial position available in the Zr_3O structure.
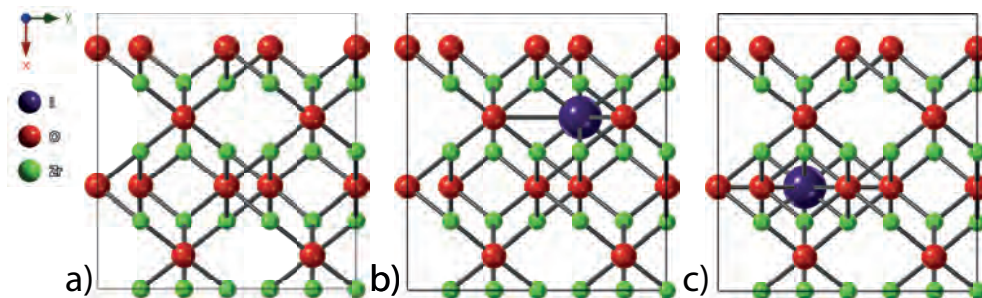
Figure 5: (a) Zr_2O structure and (b-c) the two unique octahedral interstitial positions available in the Zr_2O structure (Zr_2O-1 and Zr_2O-2).
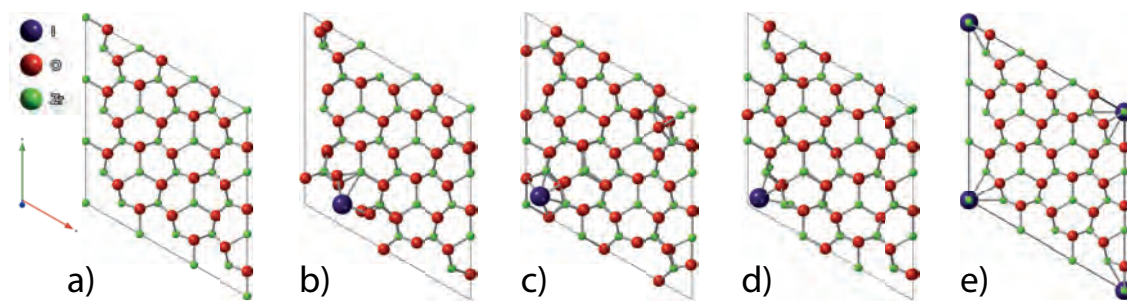
Figure 6: (a) ZrO structure and (b-e) the four unique interstitial positions available in the ZrO structure (ZrO-1, ZrO-2, ZrO-3 and ZrO-4 respectively).
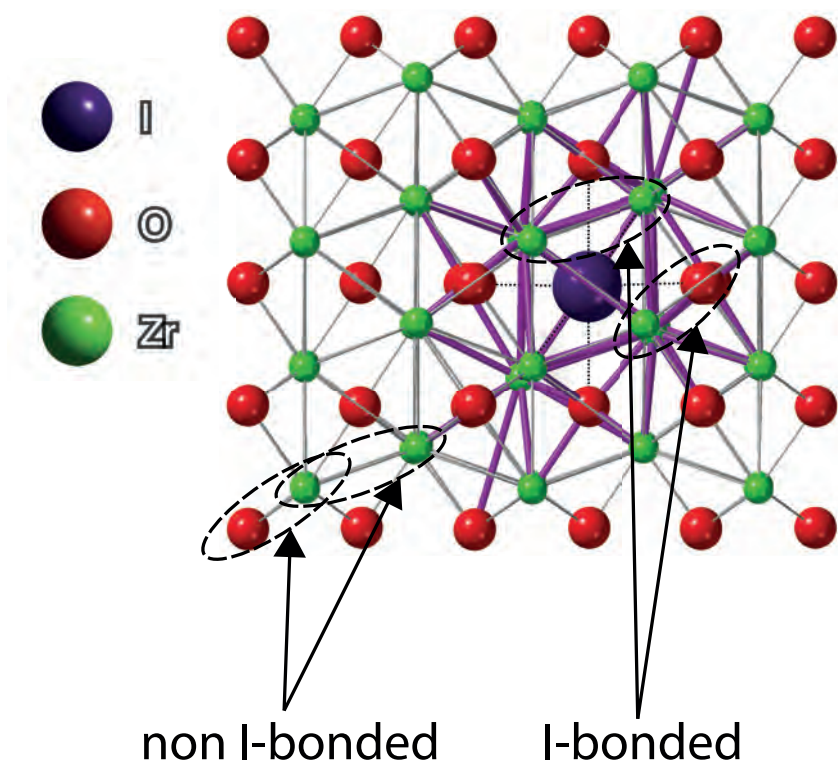
Figure 7: Illustration of the atoms analysed in the bond population analysis performed: bonds that contain at least an atom in the first shell around the iodine defect are termed *I-bonded* and colored purple and the rest are termed *non I-bonded*.
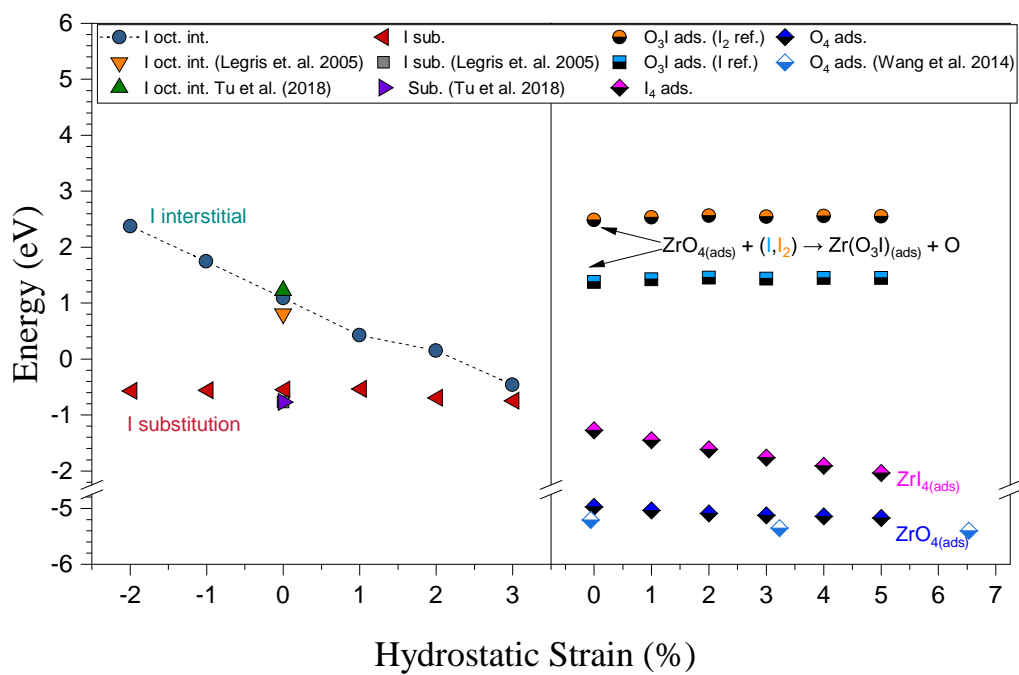
Figure 8: Formation energy of a single iodine octahedral interstitial or substitutional defect in pure zirconium as a function of hydrostatic strain (left panel) and comparison to I, O and O+I adsorption energies (right panel).
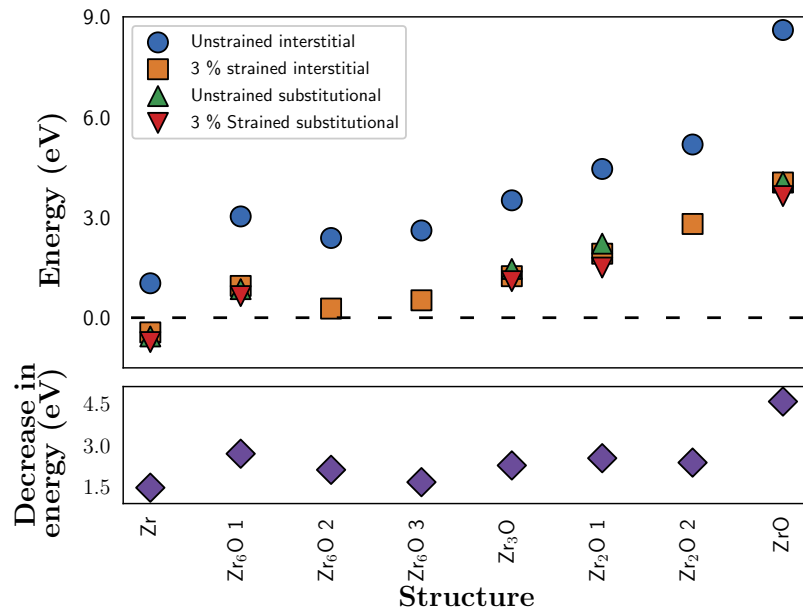
Figure 9: (top) Formation energies of the lowest energy iodine interstitial and substitutional defect in both unstrained and 3 % hydrostatic tensile strained zirconium, Zr_6O, Zr_3O, Zr_2O and ZrO. (bottom) The magnitude of the decrease in iodine interstitial defect formation energy due to the 3 % applied hydrostatic tensile strain ($E_{strained} - E_{unstrained}$).
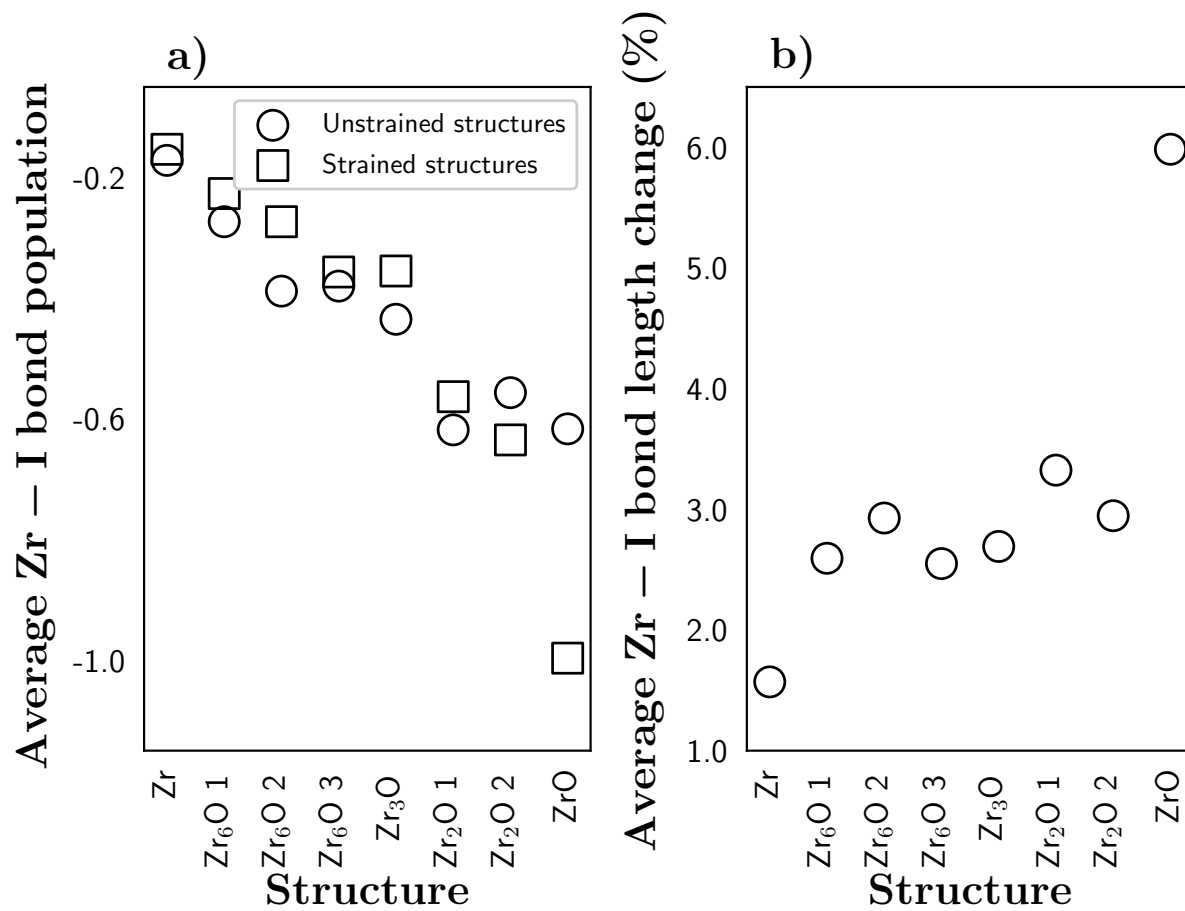
Figure 10: (a) Zr-I bond population analysis and (b) Zr-I bond length analysis for unstrained and 3 % hydrostatically tensile strained structures for iodine in interstitial sites.
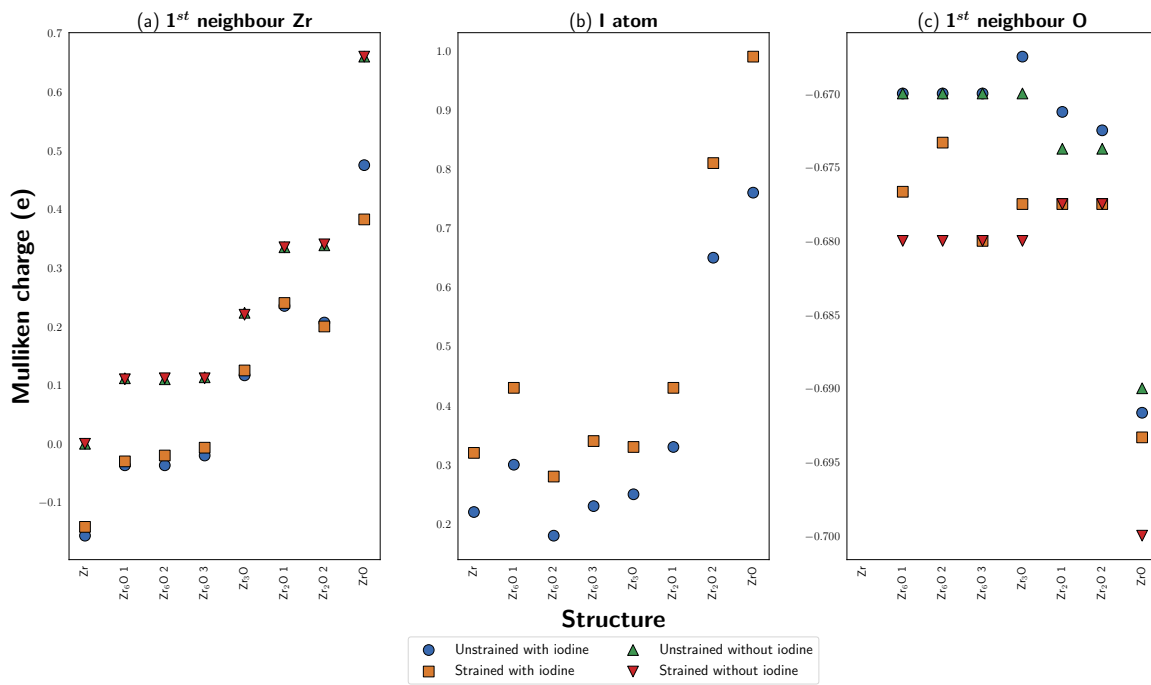
Figure 11: Mulliken charges for the 1st neighbouring Zr atoms (average), I atom and 1st neighbouring O atoms (average) in each of the structures.
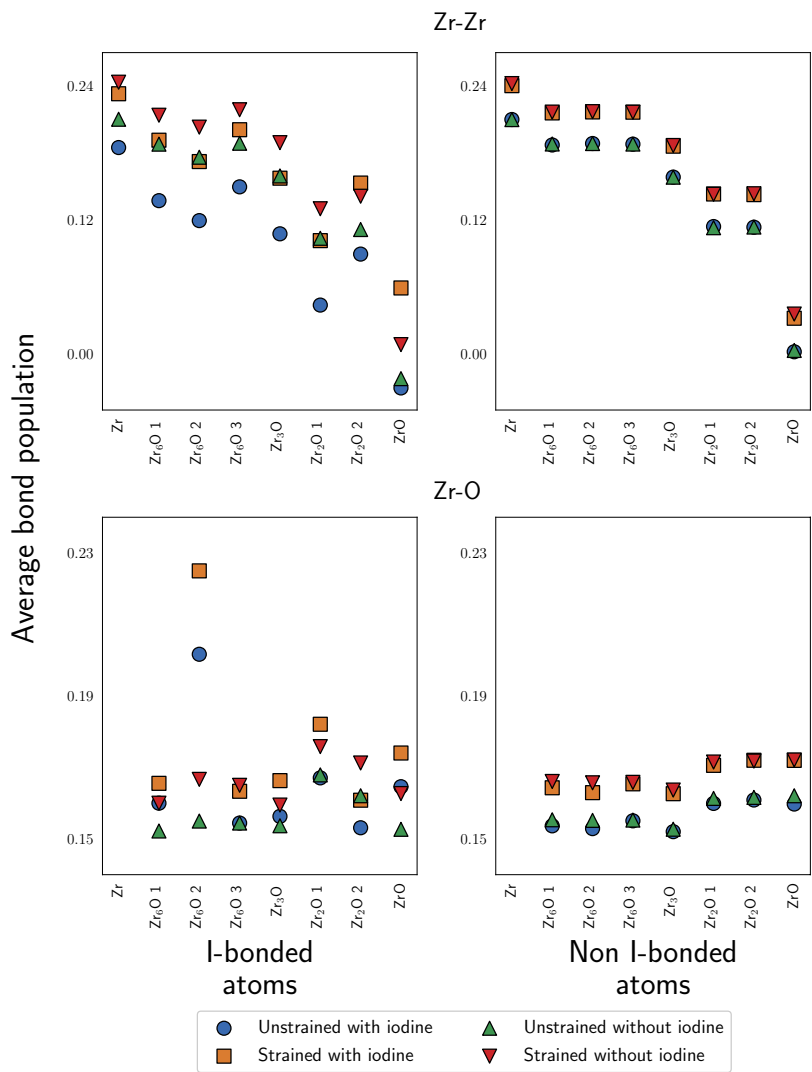
Figure 12: Zr-Zr and Zr-O bond population analysis for unstrained and 3 % hydrostatically tensile strained structures for a single iodine interstitial defect.
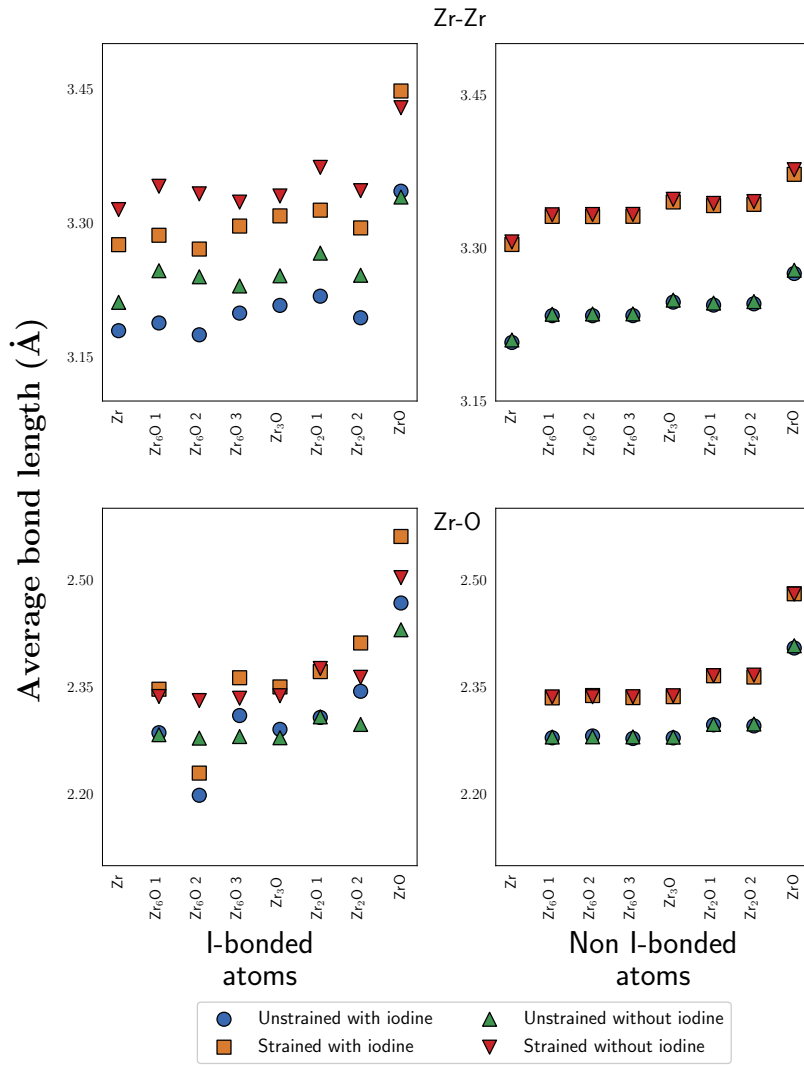
Figure 13: Zr-Zr and Zr-O bond length analysis for unstrained and 3 % hydrostatically tensile strained structures for a single iodine interstitial defect.
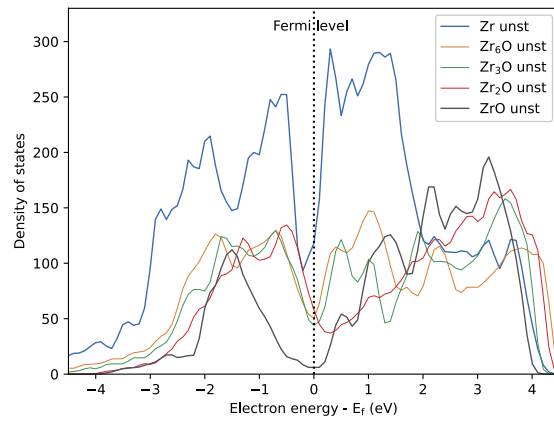
Figure 14: Density of states for bulk Zr, Zr_6O, Zr_3O, Zr_2O and ZrO showing highest density of states, around the Fermi level, for Zr and progressively less states as oxygen content increases.
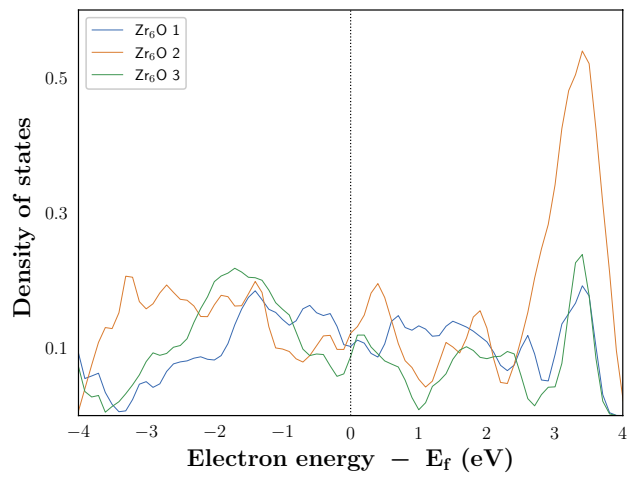
Figure 15: PDOS for the iodine interstitial atom in the 3 % tensile hydrostatic strained Zr_6O in the three positions labelled Zr_6O-1, Zr_6O-2 and Zr_6O-3.